Hydrodynamic Radius Determination of Tau and AT8 Phosphorylated Tau Mutants: A Combined Simulation and Experimental Study

Cynthia Lohberger[1*], Jules Marien[4*], Clarisse Bridot[2], Chantal Prévost[4], Diane Allegro[1], Mario Tatoni[3], Isabelle Landrieu[2], Caroline Smet-Nocca[2], Sophie Sacquin-Mora[4#] and Pascale Barbier[1#]

1. Aix Marseille Univ, CNRS, Institut de Neurophysiopathologie, Marseille, France
2. Université de Lille, INSERM, Lille, France
3. Aix Marseille Univ, CNRS, Bioénergétique et Ingénierie des Protéines, IMM, Marseille, France
4. Université Paris Cité, CNRS, IBPC, Laboratoire de Biochimie Théorique

∗ first-authors

corresponding authors

ABSTRACT

This study investigates the effect of multiple phosphorylations of the Intrinsically Disordered Protein (IDP) tau on its hydrodynamic radius (Rh). Hyperphosphorylated tau is notably implicated in Alzheimer's disease The kinases responsible for adding phosphate groups are highly involved in the regulation of biological processes such as cell division, cell signalling, and apoptosis and, particularly, in the development of Alzheimer's disease, especially those recognized by the AT8 antibody. The main objective of this work is to understand how phosphorylation at the AT8 site affects the conformation and dynamics of the tau protein through the study of its hydrodynamic radius. To achieve this, we used a tau protein mutant with all phosphorylation sites mutated to alanine except those recognized by the AT8 antibody to achieve a specific phosphorylation pattern. The phosphorylation of this mutant was performed, firstly, by incubation with CDK2/ cyclin A kinase to obtain a first phosphorylated state, termed p-state 1 (serine at positions 202 and threonines at position 205 and 212 are phosphorylated), and secondly by incubation with CDK2/cyclin A kinase followed by GSK3β kinase to obtain a phosphorylated state

termed call p-state 2 (serines 198 and 208 are phosphorylated in addition to the three previously described). The Rh of each sample was measured experimentally by dynamic light scattering (DLS) and analytical ultracentrifugation (AUC), and simulated using a new simulation model, pCALVADOS, combining the CALVADOS 2 model for IDPs with parameters for phosphorylated residues. We find that both wild-type tau and AT8-phosphorylated Tau mutants exhibit a relatively monodisperse distribution in solution suggesting that phosphorylations do not significantly alter the overall size of the conformational ensemble of tau. Our calculations of Local Curvatures and Local Flexibilities confirm that the mutations made on the tau

sequence to perform selective phosphorylations do not significantly impact local dynamics, which is corroborated by several experimental results. We also identify a local stiffening and extension of the AT8 epitope that is proportional to the number of phosphorylations. Interestingly, phosphorylations do not just affect the immediate AT8 area. We also report contact losses at a distance, with a noticeable directionality pointing towards the N-terminal end of the monomer, which could have functional implications for the phosphorylated Tau protein. The study paves the way for future research on the structure-function relationship of Tau and the role of phosphorylation in neurodegenerative diseases.

Keywords: Molecular dynamics, tau protein phosphorylation, IDP, Alzheimer disease, hydrodynamic radius, AT8 epitope, coarse-grained force field

INTRODUCTION

Alzheimer disease (AD) is defined by the presence of two biomarkers, an accumulation of extracellular fibrils of β-amyloid peptide called amyloid plaques and intraneuronal inclusions made of tau protein called neurofibrillary tangles, and neurodegeneration [1]. The neurofibrillary tangles contain filaments of hyperphosphorylated tau proteins. Tau is an intrinsically disordered protein belonging to the microtubule-associated protein family [2]. The physiological role of tau in stabilizing axonal microtubules, thereby ensuring proper neuronal activity, is mediated by its interaction with tubulin via the C-terminal MicroTubule-Binding Domain (MTBD) and a region within the proline rich domain (PRD) [3]. While phosphorylation regulates this physiological function, it is also a critical factor in the pathological aggregation of tau into neurofibrillary tangles.

In the central nervous system, tau exists as six isoforms ranging from 352 to 441 amino acids, generated by differential splicing resulting in variations in the N-terminal domain (0N, 1N, 2N) combined with different numbers of MTBD repeats that are composed of three or four imperfectly repeated sequences of 18 residues (3R, 4R) [4]. Phosphorylation within the PRD has been shown to be involved in Alzheimer's disease (AD) [5].

Simulating long IDPs via Molecular Dynamics (MD) has proven to be a significant challenge due to their rugged conformational space and their large fluctuations in size. Coarse-grained models are promising attempts to generate Conformational Ensembles (CoE) at low computational cost compared to all-atom simulations. A popular type of force fields are ones based on the HydroPhobicity Scale (HPS) model by Kapcha and Rossky [6], among which the machine-learned CALVADOS FF is becoming a staple in the field [7]. The second version of CALVADOS was released

in 2022 with improvements regarding dependency on temperature and salt concentration [8], and was recently used on a large-scale study of the Intrinsically Disordered Regions (IDRs) of nearly all of the human proteome [9]. Its capacity to generate protein conformational ensembles at low computational cost and its easy implementation in a Google Colab (https://github.com/KULL-Centre/_2023_Tesei_IDRome/blob/main/IDRLab.ipynb) makes CALVADOS a valuable tool to study IDPs as long as tau. Moreover, since its training set contains the tau protein and since it has already been used successfully to predict hydrodynamic radii values by Pesce et al. [10], we deemed it a reliable forcefield to use as a base for our study. CALVADOS however does not include parameters for phospho-residues yet. We therefore extracted them from the model by Perdikari et al which is also an HPS-based model [11]. Since this kind of “mix-and-match” approach regarding parameters of phospho-residues has proven successful in the past for all-atom force fields, we assumed it might also be the case for coarse-grain approaches, as long as the base model is the same. We named this combination pCALVADOS and performed simulations matching the experimental sequences.

Assessing the local dynamics of an IDP is a complex task as standard alignment-based methods such as RMSD and RMSF lose all meaning in disordered systems. We therefore employed new metrics specifically tailored for IDPs and IDRs (Proteic Menger Curvature, Local Curvature and Local Flexibility)[12] and found a good qualitative agreement with the experimental results.

In this study, we focus on pathological phosphorylation of Tau recognized by the AT8 antibody at Serine 202, Threonine 205, and Serine 208 [13]. We chose these specific phosphorylation sites as the AT8 antibody is commonly used in post-mortem diagnosis of Alzheimer's disease and its staining on patients' brains correlates with the different Braak stages defining the disease progression [14]. Most

studies investigating the effects of tau phosphorylation on its interaction with tubulin have either used tau peptides, which neglects complex molecular interactions, or fully phosphorylated tau, leading to potential misinterpretations due to multiple phosphorylation sites. In this study, we employ the full-length tau isoform mutated on 16 phospho-sites phosphorylated *in vitro* by specific kinases, to allow us to specifically study the impact of three and five phosphorylations. We define these phosphorylation states as p-state 1 (pSer202 + pThr205 + pThr212) and p-state 2 (pSer198 + pSer202 + pThr205 + pSer208 + pThr212) (Figure 1) and compare them to non-phosphorylated tau. Structural studies have revealed that p-state 1 induces a local conformational change characterized by a kink at residue 207. Interestingly, this kink is disrupted by the additional phosphorylation of serine 208 (p-state 2) [15,16]. Furthermore, while pS202/pT205 in p-state 1 is unable to form oligomers, the triple phosphorylation pS202/pT205/pS208 in p-state 2 exhibits a propensity to form pathological oligomers [15,16]. These findings suggest that the phosphorylation of serine 208 plays a critical role in promoting tau aggregation and detachment from microtubules, thereby contributing to the pathogenesis of neurodegenerative diseases by local conformational modification. To evaluate the effect of this local conformational change on the global conformation and dynamic of Tau, we combined simulation and experimental study to determine the effect of multiple phosphorylations on the hydrodynamic radius of Tau.

MATERIALS AND METHODS

WT tau purification

Tau purification has been already described [17,18] but we will summarize the main step here. The tau 441 (hTau40, 2N4R) gene was cloned into a pET-3d vector. This plasmid was transformed into *E. coli* BL21(DE3) cells. The bacteria were grown

overnight in a LB medium containing 100 µg.mL^{-1} ampicillin for antibiotic selection. After dilution, the culture was supplemented with 20 mM glucose to promote growth. The tau protein production was induced with 0.75 mM isopropyl 1-thio-β-D-galactopyranoside (IPTG) and cells were further incubated for 2 hours 30 at 37 °C. The cells were harvested by centrifugation at 5000*x g* for 10 mins at 4 °C and then suspended in 2-(N-Morpholino)ethanesulfonic acid 45 mM, Triton X 100 8 mM, DTT 1mM. The cell suspension was disrupted using a French press, releasing the cellular contents. The lysate was then heated to denature unwanted proteins and clarified by centrifugation at 30000*x g* during 30 min, separating soluble proteins from cell debris. The supernatant containing tau was purified using an cation-exchange chromatography column HiTrap SP-HP 5 mL (Cytiva). The column was equilibrated with 45 mM MES, at pH 6.5, and loaded with tau and then a salt gradient was applied. Tau protein bound to the column at a specific salt concentration and was then eluted with a higher salt solution (0.25 M of NaCl). The eluted fractions containing tau were pooled together. To remove excess salt, the pooled fractions were dialyzed overnight against pure water. The purity of the proteins was verified by SDS-PAGE (figure SI-7). Finally, the Tau protein solution was lyophilized (freeze- dried) for storage.

Purification and characterization of phosphorylated and non-phosphorylated mutants

The tauAT8 mutant protein corresponds to a mutated form of tau 2N4R isoform in which 16 Serine/Threonine were mutated into Alanine to prevent phosphorylation while keeping those of the AT8 phospho-epitope (S202, T205, S208), S198 and T212 [16] (Figure1, Figure SI-6). The mutant was obtained by gene synthesis with optimization of codons for *E. coli* expression and cloned into the pET15b vector

(Novagen) into NcoI/XhoI allowing removal of the sequence coding for the

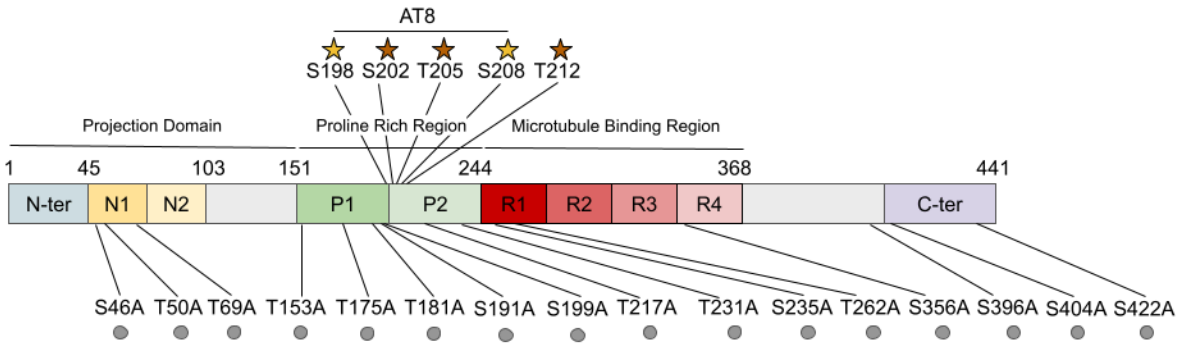

Figure 1: *Domain organization and phosphorylation sites of wild-type Tau and Tau mutants designed to investigate the role of specific phosphorylation events in Alzheimer's disease. The gray circles represent the 16 sites serines/threonines mutated into alanine. p-state 1: Serine 202 and threonines 205 and 212 are phosphorylated indicated by brown stars. p-state 2: Serines 198 and 208 are additionally phosphorylated compared to p-state 1 indicated by yellow stars.*

polyhistidine tag. Tau AT8 mutant was prepared under conditions described previously for wild-type Tau [19]. Briefly, BL21(DE3) *E. coli* strains transformed with Tau mutants were grown in M9 minimal medium enriched with ^{15}N as nitrogen source for uniform isotopic ^{15}N-labelling (6g Na_2HPO_4, 3g KH_2PO_4, 0.5g NaCl, 4g glucose, 1g $^{15}NH_4Cl$, 0.5g ^{15}N-ISOGRO®, 1 mM $MgSO_4$, 100 µM $CaCl_2$, 100 mg ampicillin per liter) at 37°C. The protein expression was induced by addition of 0.5 mM IPTG for 3 hours. The protein was purified by cation exchange chromatography after heating the soluble extract at 80°C for 15 minutes. Then, the fractions were purified by reverse phase HPLC. The fractions containing the full-length TauAT8 protein are lyophilized, desalted into 20 mM NaPi buffer pH=6.5, dialyzed in water at 4°C overnight, and lyophilized again.

Phosphorylated forms of TauAT8 mutant were produced either by phosphorylation with recombinant CDK2/cyclinA (p-state 1, pSer202 + pThr205 + pThr212) or by a

sequential phosphorylation with CDK2/cyclinA and GSK3β kinases (p-state 2, pSer198 + pSer202 + pThr205 + pSer208 + pThr212) as described in ref. [19].

The tau AT8 mutant and its two phosphorylated forms were analyzed by MALDI-TOF MS (Axima Assurance, Shimadzu) in a linear positive ion mode with sinapinic acid matrix after ZipTip®-C_4 desalting (Millipore). For the calculation of overall phosphorylation levels, a m/z increment of +80 Da per phosphate group was measured and confirmed by SDS-Page (Figure SI-7)

Determination of concentration of WT tau and tau AT8 proteins by spectrophotometry

Lyophilized WT tau, tau AT8 mutant and its phosphorylated p-state 1 and p-state 2 forms were resuspended in 500 µL of 20 mM NaPi pH 6.5 buffer containing 1 mM TCEP. Following centrifugation for 10 min at 1500*x g*, the supernatant was diluted to an appropriate concentration for UV-Vis spectroscopy. The absorbance spectra were recorded from 250 to 600 nm using a JASCO-V750 spectrophotometer. To account for light scattering, a mathematical model was employed to correct the absorbance values (y= a+bx.exp(-c)). Tau concentration was determined using an extinction coefficient of 7700$M^{-1}.cm^{-1}$ at 280 nm.

Hydrodynamic radius determination by Dynamic Light Scattering (DLS)

Dynamic Light Scattering (DLS) with Malvern Zetasizer Pro equipment was employed to investigate the size distribution and hydrodynamic radius (Rh) of Tau WT, Tau AT8 mutants and its phosphorylated p-state 1 and p-state 2 forms. Samples were prepared in a 20 mM NaPi buffer pH 6.5,1 mM TCEP and analyzed at 20°C at different protein concentrations (between 1 and 40 µM). The solvent refractive index and viscosity were set to 1.33 and 1.002 mPa·s, respectively. Data

were collected using the Hückel approximation, with 150 measurements per sample. The hydrodynamic radius of the particles was determined using the Stokes-Einstein equation: $Rh = k_B T / (6\pi\eta D)$, where *Rh* is the hydrodynamic radius, k_B is the Boltzmann constant, *T* is the temperature, *η* is the viscosity of the solvent, and *D* is the diffusion coefficient. The diffusion coefficient was calculated from the measured relaxation time (τ) using the following relationship: $\tau = 1/(q^2 D)$, where *q* is the scattering vector.

To determine the distribution of particle sizes, the data were analyzed using two methods: The *Hydrodynamic Volume Analysis*, providing information about the relative abundance of particles with different sizes; and the *Scattered Light Intensity Analysis*, providing a more accurate determination of the hydrodynamic radius of the dominant species in the sample.

Hydrodynamic radius determination by Analytical UltraCentrifugation (AUC)

Sedimentation velocity experiments for WT Tau, Tau AT8 mutants and its phosphorylated p-state 1 and p-state 2 forms were carried out on a Beckman Optima Analytical UltraCentrifuge equipped with absorbance and interference optics. Samples were centrifuged at 60 000 rpm at 20°C into 12 mm double-sector aluminum centerpieces. The absorbance scans were acquired at 275 nm. The apparent sedimentation coefficients were determined using the SEDFIT software [20]. To account for the effects of temperature and solvent viscosity, these coefficients were corrected to standard conditions (20°C, in water) using the SEDNTERP software [21]. The partial specific volume of WT Tau and Tau mutant was calculated to be 0.736 $mL.g^{-1}$ and 0.7286 $mL.g^{-1}$ respectively (SEDNTERP software).

The solvent density and viscosity were calculated using SEDNTERP and were

found to be 1.0029 $g.mL^{-1}$ and 0,01002 poise, respectively. The hydrodynamic radius was obtained using the definition of the sedimentation coefficient and the following Svedberg equation (1):

$$Rh=\frac{M(1-\bar{v}\rho)}{6\pi\eta Na\ S} \quad (1)$$

Where M is the molecular mass, $\bar{v}$ is the partial specific volume, ρ is the solvent density, η is the viscosity of the solvent, Na the Avogadro's number and S the sedimentation coefficient.

Statistics

In order to compare the different forms of tau, we aim to analyze the variations in their hydrodynamic radii and sedimentation coefficients. Their confidence intervals were determined as described below. We first determined the variance of the intercept of the linear regression b obtained both in DLS and sedimentation velocity experiments with equation (2):

$$S_b^2=\frac{S_y^2(1-r^2)\sum x_i^2}{S_x^2 n(n-2)} \quad (2)$$

S^2_b is the variance of the intercept b; S^2_y is the variance of the y (apparent Rh or sedimentation coefficient Sapp,20,W); S^2_b is the variance of the x (the concentration); r^2 is the squared correlation coefficient of the linear regression and n the number of points. Then, the confidence interval was calculated using equation (3):

$$b\pm t_{n-2,\alpha}\sqrt{S_b^2} \quad (3)$$

Where t is the student parameter obtained for the n-2 degree of freedom and α is the risk (=0.05) with the Bonferroni correction.

Molecular dynamics simulations: pCALVADOS implementation

We performed MD simulations in order to obtain Conformational Ensembles (CoEs) of Tau wild-type and the phosphorylated and non-phosphorylated mutants. To do so we assembled a new parameter set, pCALVADOS, by merging the parameters of CALVADOS 2 [8] with those of doubly charged phosphoserine, phosphothreonine, and phosphotyrosine described in Perdikari et al (see Table S1 in ref. [11]). The resulting parameter set is provided in the following CSV file: https://github.com/Jules-Marien/Articles/blob/main/_2025_Lohberger_Marien_pCALVADOS/pCALVADOS/pCALVADOS_residues_and_phosphoresidues.csv

Phosphoresidues were named based on the Amber nomenclature for the 3-letter denomination and were each given an arbitrary letter as a 1-letter denomination (SEP = B, TPO = J, PTR = O). One simply needs to replace S, T or Y in the sequence by their phospho-residue 1-letter equivalent in order to launch a simulation with phosphorylations. The IDRLab Jupyter Notebook designed by Tesei et al was modified to account for pCALVADOS and to run our simulations of all mutants and p-states. (IDRLab : https://github.com/KULL-Centre/_2023_Tesei_IDRome/blob/main/IDRLab.ipynb, pCALVADOS notebook : https://github.com/Jules-Marien/Articles/blob/main/_2025_Lohberger_Marien_pCALVADOS/pCALVADOS/pCALVADOS_notebook.ipynb).

The temperature was set at 300K and ionic strength to 0.02 mol.L^{-1} to match the DLS experiment. Termini were charged and histidines were kept neutral. Trajectories were run for 100100000 steps, corresponding to 1001 ns. The first nanosecond was discarded as equilibration, since the protein chain starts as a straight string of beads. Frames were sampled every 5000 steps, providing a CoE of 20000 frames evenly spaced by 50ps.

From coarse-grain to all-atom

pCALVADOS, as a coarse-grained forcefield, represents each residue as a single bead. It could however be interesting to recover some of the information provided by side-chains, especially as we are interested in phosphorylations. Tesei et al. already proposed a protocol based on the PULCHRA program to convert a CALVADOS trajectory to an all-atom trajectory [22]. PULCHRA is, however, not capable of converting phospho-residues to all-atom representation, and simply provides canonical residues instead. We therefore designed a new protocol to recover all-atom trajectories. Scripts are available at https://github.com/Jules-Marien/Articles/tree/main/_2025_Lohberger_Marien_pCALVADOS/Scripts_CG_2_AA

At first, PULCHRA was used to generate non-phosphorylated all-atom trajectories. A TCL script was then used in combination with VMD to add the proper phosphorylations using CHARMM patches [23] and generate a topology file per conformation. A minimization of 100 steps was performed on each resulting frame using NAMD and the CHARMM36m forcefield, constraining only the backbone heavy atoms to preserve the overall conformation [24,25]. This step allows on one hand to relax any steric and electrostatic tensions induced by adding phosphorylations and also provides a better extrapolation of the side-chains thanks to a state-of-the-art all-atom force field. The relaxed conformations were then re-assembled into an all-atom phosphorylated trajectory. The same protocol was followed for non-phosphorylated systems for consistency. Both raw coarse-grain trajectories and relaxed all-atom trajectories are available on Zenodo: https://doi.org/10.5281/zenodo.14900596

Rh simulation analyses and new metrics

All analyses were performed using Python scripts based on the MDAnalysis and MDTraj packages [26-28]. Hydrodynamic radii were calculated using the Kirkwood-Riseman and the Nygaard methods described by Pesce et al. [10], inspiring ourselves from the following scripts: https://github.com/KULL-Centre/papers/tree/main/2022/rh-fwd-model-pesce-et-al/Rh_scripts. The linear fit of experimental Rh was performed with the curve_fit function of the scipy.optimize module [29].

Contact maps were computed by defining a contact as two heavy atoms from two different residues within 5 Å of one another, then calculating the percentage of simulation time during which a pair of residues is in contact. Proteic Menger Curvatures (PMCs), Local Curvatures (LCs) and Local Flexibilities (LFs) were calculated using the previously published Python module [12]:

https://github.com/Jules-Marien/Articles/blob/main/_2024_Marien_nPcollabs/Demo_and_scripts_Proteic_Menger_Curvature/MODULE_Proteic_Menger_Curvature.py. Convergence of the simulations is discussed in the Supplementary materials (Figure SI-0).

RESULTS

Production of phosphorylated and non-phosphorylated mutants

To study the specific effects of tau phosphorylation at the AT8 epitope, a tau protein mutant was created with 16 phosphorylation sites mutated into alanine except those recognized by the AT8 antibody (Figures 1 and SI-6). The mutant is then turned into two different phosphorylation states. p-state 1 is achieved by incubating the tau mutant with CDK2/cyclin A kinase, which results in the phosphorylation of serine at positions 202 and threonine at position 205 and 212. p-state 2 is achieved by incubating the tau mutant with CDK2/cyclin A kinase followed by GSK3β kinase,

which leads to two additional phosphorylations on serines 198 and 208. The 16 phosphorylation sites have been identified and characterized using Nuclear Magnetic Resonance (NMR) spectroscopy on WT tau phosphorylated by CDK2/cyclin A kinase followed by GSK3β kinase [19]. By creating these two distinct phosphorylation states, we can investigate the effects of different phosphorylation patterns within the AT8 epitope without interference from other phosphorylation events.

Determination of the hydrodynamic radius

To investigate the hydrodynamic properties of tau and of the non-phosphorylated and phosphorylated AT8 mutants, we performed Dynamic Light Scattering (DLS) measurements. The first objective is to assess whether the tau mutant is a good proxy for wild-type tau. The hydrodynamic radii are obtained by plotting the measured hydrodynamic radius as a function of various protein concentrations and extrapolated with a linear regression to infinite dilution (Figure 2). Then, the y-intercept of the linear regression line is interpreted as the estimated hydrodynamic radius (Rh) of the protein at concentration 0.

WT Tau exhibited a Rh of 4.92nm with a confidence interval of 1.25 nm (4.92 ± 1.25 nm) in agreement with this obtained previously [30,31]. The non- phosphorylatable mutant displayed a Rh of 4.61 ± 1.46 nm. The observation that the mutant exhibits a hydrodynamic radius comparable to that of wild-type Tau suggests that this mutant provides a suitable model for investigating AT8-specific phosphorylation. The p-state 1 construct has a Rh value of 5.71 ± 1.32 nm and the p-state 2 displays a Rh of 4.91 ± 1.75 nm. The confidence intervals obtained for the four different samples of tau overlap, indicating no significant difference in the

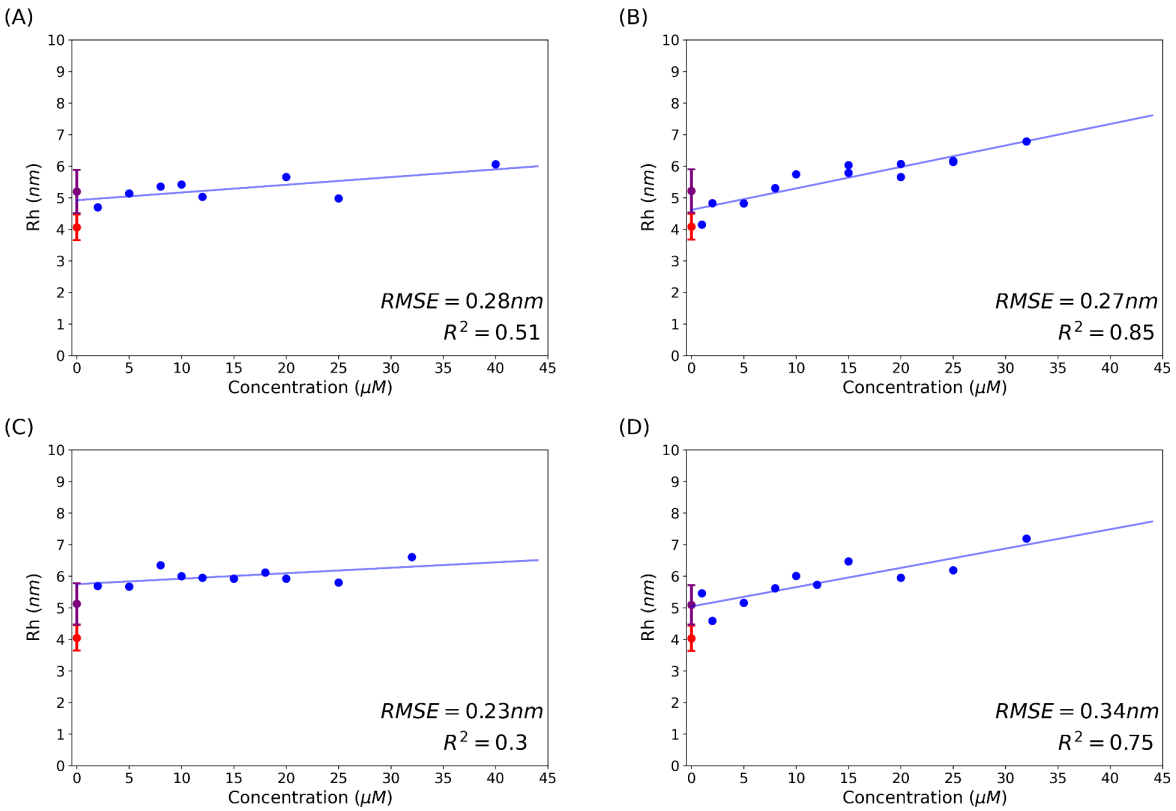

Figure 2: *Hydrodynamic radius of WT tau, non-phosphorylated mutant, p-state 1 mutant and p-state 2 mutant as a function of protein concentration. Experimental measurements from DLS and the linear fit from the experimental data are indicated in blue. Computed values from the pCALVADOS simulations are in red (Kirkwood-Riseman method) and in purple (Nygaard method) with their associated standard deviations. (A) Wild-type Tau (concentration range 2-40 μM). (B) Unphosphorylated Tau mutant (concentration range 1-32 μM). (C) Tau mutant in p-state 1 (pSer202 + pThr205 + pThr212) (concentration range 2-32 μM). (D) Tau mutant in p-state 2 (pSer198 + pSer202 + pThr205 + pSer208 + pThr212) (concentration range 1-32 μM).*

hydrodynamic radii. Nor the alanine mutation, nor the degree of phosphorylation have an impact on Tau conformation.

A second method was used to confirm the hydrodynamic radius values. Velocity experiment in analytical ultracentrifugation allows us to determine the sedimentation

coefficient that reflects both the mass and the conformation of a protein. The results obtained with the non-phosphorylatable tau mutant are represented in Figure 3. The sedimentation coefficient distribution C(S) shows three peaks corresponding to the presence of three molecular species in solution. A small peak with a sedimentation coefficient of 1.48 ± 0.1 Svedberg (S) is observed, a second one largely represented with a sedimentation coefficient of 2.4 ± 0.1 S represents the monomeric form of tau, and a very little peak at approximately 4S indicating tau aggregation. As for DLS experiments, the apparent sedimentation coefficient $S_{app,20,W}$ of the main species was plotted in function of various concentrations of tau and analyzed by linear regression to obtain the value at infinite dilution ($S^0_{W,20}$). We obtained a sedimentation coefficient of 2.36 ± 0.43 S, 2.35 ± 0.36 S, 2.30 ± 0.82 S and 2.45 ± 0.26 S for Wild-type tau, unphosphorylated mutant, mutant in p-state 1 and p-state 2 respectively. The confidence intervals obtained for the four different

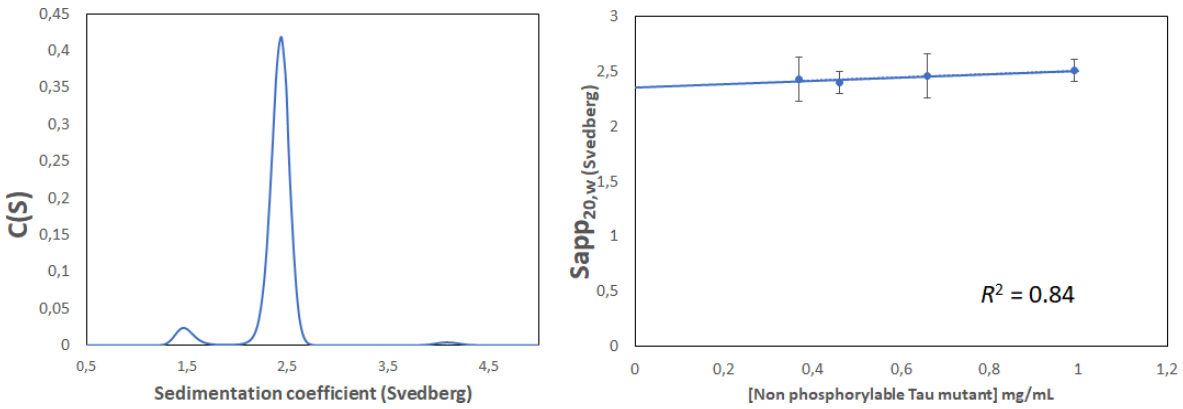

Figure 3: *Determination of the sedimentation coefficient of non-phosphorylated mutant by sedimentation velocity experiment in analytical ultracentrifugation. (A) Sedimentation coefficient distribution determined by Sedfit analysis of 0.46 mg/mL of unphosphorylated mutant. (B) apparent sedimentation coefficient of unphosphorylated mutant as a function of protein concentration (concentration range 0.3-1 mg/mL).*

samples of tau overlap, indicating again no significant difference in the sedimentation coefficients. This points towards a lack of effect of the mutations and of the phosphorylation state of tau. Values of hydrodynamic radii were estimated from the sedimentation coefficient with the Svedberg equation (see Materials and methods). The obtained values are in accordance with those measured directly by DLS and confirm the absence of effect of the mutations and of phosphorylations on the CoE of tau.

Values for the hydrodynamic radius (Rh) were computed using the brute-force Kirkwood-Riseman (KR) method and the empirical Nygaard method. According to Pesce et al, the latter should be better than the former in terms of agreement with the experimental value of 5.20 +/- 0.20 nm obtained by NMR diffusion experiments [30]. It is indeed what is observed with the Nygaard method, which returns a computed Rh value of 5.2 +/- 0.7 nm, while the KR method underestimates the value (4.1 +/- 0.4 nm). This is to be expected as the Nygaard method tackles the lack of consideration of solvation effects by the KR method, and is specifically tailored for IDPs [32]. The Rh values at 0 μM are very similar between all systems, regardless of the sequence or the phosphorylation state, in agreement with experimental results, with only the slope of the fit varying. This could imply that if there is an effect on intramolecular interactions, it would be very transient and/or very local. All the results of experimental and simulated Rh determination were summarized in Table 1.

The hydrodynamic radii obtained using different methods are consistent within this study and others, suggesting a good reliability of the results [30]. The relatively high confidence interval obtained by DLS and AUC suggest a certain heterogeneity in the particle populations, which could be due to the presence of

Protein	Kirkwood-Riseman (KR)	Nygaard method Rh	DLS experimental Rh	AUC experimental Rh
WT tau	4.1 ± 0.4 nm	5.2 ± 0.7 nm	4.92 ± 1.25 nm	4.47 ± 0.82 nm
non phosphorylated tau mutant	4.1 ± 0.4 nm	5.2 ± 0.7 nm	4.61 ± 1.46 nm	4.51 ± 0.69 nm
tau mutant p-state 1 (pSer202, pThr205, pThr212)	4.0 ± 0.4 nm	5.1 ± 0.7 nm	5.71 ± 1.32 nm	4.63 ± 1.65 nm
tau mutant p-state 2 (pSer198, pSer202, pThr205, pSer208, pThr212)	4.0 ± 0.4 nm	5.1 ± 0.7 nm	4.91 ± 1.75 nm	4.37 ± 0.46 nm

Table 1 : *Hydrodynamic radius of wild-type and phosphorylated Tau variants as determined by DLS, AUC and pCALVADOS simulations.*

different protein species (monomers, oligomers) or to different conformations of the Tau protein. Indeed, three species were evidenced in the AUC experiment.

Local dynamics

The transient nature of intramolecular interactions can be investigated via the simulated trajectories using contact maps and secondary structure calculations (Figures SI-1, SI-2,SI-3). All contacts made between two residues in all systems are present less than 10% of the simulated time, indicating a very dynamic behavior of the peptide chain (Figures SI-1 and SI-2). A notable exception is contacts within a 3-residue span, which can exist for more than 20% of the time. This could point towards transient secondary structuration. We therefore calculated the DSSP profile of each system and observed no secondary structure except transient turns (Figure SI-3). This result must however be nuanced by the nature of the calculation which uses hydrogen bonds to detect possible structuration, and the translation to all-atom of the coarse-grained simulations might induce biases. We still noticed that, while the unphosphorylated systems display very similar DSSP profiles (figures SI-3A and SI-3B), the phosphorylated systems show an overall decrease in turns near the epitope site (Figures SI-3C and SI-3D). This hints to a possible local elongation of the backbone due to phosphorylations.

To assess the impact of the mutations and of the phosphorylations, we decided to use the wild-type Tau simulation as a reference. We subtracted the contact map of the wild-type to the mutant and its different p-states to highlight which contacts are impacted. Figure 4A displays the difference between the unphosphorylated mutant and tau wild type. Long-range interactions are barely modified by the alanine mutations with differences compared to reference of less than 1%, and local interactions (within five residues) mostly show negligible losses of contacts inferior to 5%. The comparison with the phosphorylated states, however, reveals interesting local and long-range effects. Contacts are strengthened within 50 residues of the epitope, notably with ARG170, LYS174, LYS190 and ARG194 on the N-ter side and with ARG221, LYS224, LYS225, ARG230, LYS234, LYS240 and ARG242 on the C-ter side (Figures 4B and 4C). On the other hand, and quite surprisingly, contacts are weakened at very long residue-range (up to 200 amino-acids away) when the epitope is phosphorylated, with a stronger effect on residues GLU53, ASP54, GLU55, GLU57, GLU58 and a weaker one for ASP34, GLU35, GLU38, GLU73, GLU104 and GLU105. The effect is also only present for the N-terminal part of tau, which indicates that the unphosphorylated epitope has a preferential affinity with it.

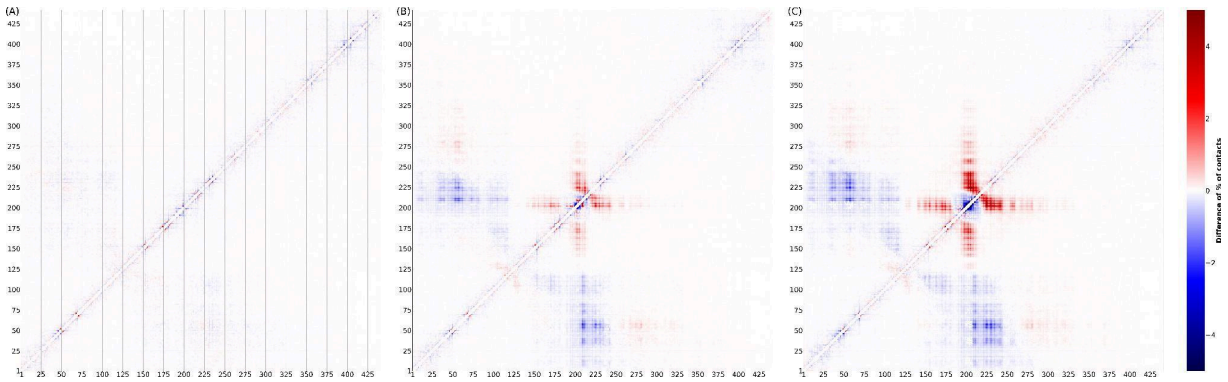

Figure 4: *Difference of percentages of contacts per residue pairs between the unphosphorylated mutant (A), the mutant in p-state 1 (B), the mutant in p-state 2 (C) and the tau wild type.* Contact gains are in red, contact losses are in blue.

These contact differences are increased as the number of phospho residues increase (Figure 4C), suggesting that they are probably electrostatic in nature.

Local curvatures and flexibilities

Next, we calculated the Proteic Menger Curvatures (PMCs), Local Curvatures (LCs) and Local Flexibilities (LFs) of the residues of each system. Authors previously introduced these metrics to characterize bending of the protein backbone induced by counterion bridges in multi-phosphorylated peptides [12]. The time evolution of the PMCs reveals little changes over time, but some differences between the systems (Figure SI-4). Hence, we once again used the Tau wild-type simulation as a reference to assess the effects of the mutations and phosphorylations on the curvature and flexibility of the backbone. The comparisons of LCs and LFs do not exhibit significant differences at the sites of mutations (Figure SI-5), which supports our hypothesis that the tau mutant is a good proxy for tau in order to study phosphorylation effects. When focusing on the epitope, we observe a strong effect of phosphorylations on backbone dynamics (Figure 5). Curvatures and flexibilities are both reduced for both p-states, indicating a local stiffening and elongation of the backbone probably due to electrostatic repulsion. This effect also depends on the number of phosphorylations as LCs are only decreased by -0.025 $Å^{-1}$ for PRO203 and GLY204 for p-state 1, whereas most residues from ALA199 to PRO206 see their LC drop by more than -0.025 $Å^{-1}$ for p-state 2 (Figure 5A). The difference between p-states is even more noticeable with LFs as differences with the wild-type for PRO200 and SER210 are three times higher for p-state 2 than for p-state 1 (Figure 5B).

To summarize, pCALVADOS simulations of the backbone dynamics and derived hydrodynamic radii are in agreement with the experimental data. In both cases we

demonstrated that there is no effect on the global conformation of Tau. More interestingly, we show a reduction of the curvature and flexibility of the backbone around the AT8 epitope that could hint towards a structural role of phosphorylations for Tau.

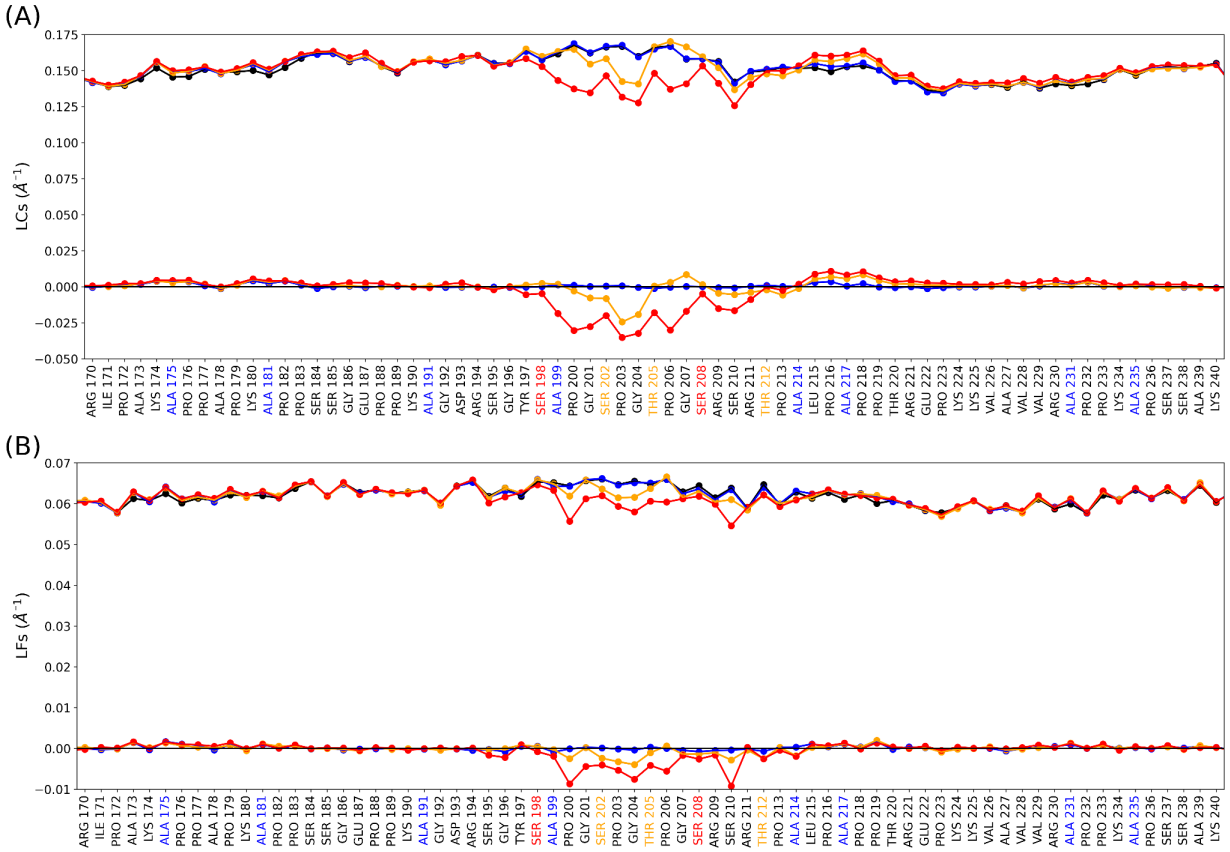

Figure 5: *Local Curvatures (A) and Local FLexibilities (B) of the AT8 epitope. Upper curves on each graph represent Local Curvatures (A) and Local Flexibilities (B) for wild-type Tau (black), the unphosphorylated mutant D (blue), the mutant in p-state 1 (orange) and the mutant in p-state 2 (red). The lower curves on each graph represent the difference with regard to the wild type. Positive values represent a gain in curvature/flexibility respectively and negative values a loss. Residues in blue have been mutated to alanine compared to Tau wild type. Residues in orange are phosphorylated in p-state 1, residues in red in p-states 1 and 2.*

DISCUSSION

Protein phosphorylation is a crucial posttranslational modification catalyzed by kinases that transfer phosphate groups from ATP to specific amino acid residues and regulates diverse processes, including cell signaling, proliferation, and apoptosis [33]. Among these kinases are the serine/threonine kinases (STKs) which constitute an important part of the human kinome, phosphorylating the hydroxyl groups of serine or threonine residues.

Tau phosphorylation is a dynamic process regulated by numerous kinases and phosphatases (enzymes that remove phosphorylation). Both enzyme types work in concert to maintain a balance of tau phosphorylation under normal physiological conditions. However, dysregulation of this balance can lead to hyperphosphorylation and contribute to tau-related pathologies. Along the 441 amino acid sequence of the longest isoform of human Tau, there are 85 potential phosphorylation sites. While the exact number of identified phosphorylation sites varies slightly depending on the source, it is generally agreed that more than 40 sites have been identified [34,35].

Alanine scanning mutagenesis is a technique often used to study the impact of amino acid substitutions on protein structure and function [36,37]. In our study, specific residues determined before by NMR to be phosphorylated by CDK2/cyclin A and GSK3-β kinases in vitro [15,16] are replaced with alanine to prevent phosphorylation. Serine and threonine are polar amino acids with a hydroxyl group (-OH) in their side chain, essential for phosphorylation. Alanine, on the other hand, has a nonpolar methyl group (-CH3), which lacks the chemical properties necessary for phosphorylation. Due to its small inert methyl side chain, and its structural similarity to serine and threonine, alanine is less likely to disrupt the overall

structure of a protein compared to other amino acids. Although the methyl side chain of alanine is hydrophobic, it can also participate in polar interactions via its amino and carboxyl groups. In many cases, the introduction of alanine at serine or threonine sites does not significantly alter the protein's hydrophobic interactions or its overall folding [37]. Although alanine mutations do not typically cause major structural changes, their impact can vary depending on the specific protein and location of the mutation. In some cases, alanine substitutions can affect protein stability or interactions with other molecules, even if overall folding remains largely unchanged. For example, surface point mutations can disrupt electrostatic interactions and affect protein stability by introducing large-scale movement that switches the beta sheet between functional (folded) and dysfunctional (unfolded) forms. 14-3-3 and Pin-1 proteins, which are regulatory proteins that interact with hundreds of phosphorylated proteins including phosphorylated Tau, illustrate the complexity of phosphorylation and its mimicry. Phosphomimetic mutations may not accurately represent the effects of phosphorylation, because the dimer-monomer balance of the phosphorylated protein is shifted more toward monomers than that of phosphomimetic mutants [38]. That is the reason why we chose to use the alanine mutagenesis to isolate the phosphorylation of interest. However, since we had to introduce several alanine mutations (Figure SI-6), we have first assessed their impact on the overall Tau conformation. DLS and AUC experimentations showed no global conformational change between the mutant and wild-type Tau indicating that the mutant is a good candidate to study the impact of AT8 phosphorylation.

IDPs such as tau lack a stable 3D structure, making them challenging to study using traditional biophysical techniques. As IDPs are often difficult to obtain in large quantities and DLS requires only small sample volumes, DLS offers a valuable tool for characterizing IDPs in solution by providing information about their size, shape,

and interactions. We decided to use a range of concentrations and perform a linear regression to determine the Rh of our proteins, because IDPs can adopt a wide range of conformations and sizes in solution, influenced by factors such as temperature, pH, and ionic strength. This conformational variability means that a fixed concentration based on mass does not correspond to a constant hydrodynamic size. The disordered nature of IDPs leads to increased interactions with the solvent, which further affects their hydrodynamic behavior [39]. These interactions can influence the effective size of the protein and complicate the interpretation of DLS data. The fluctuations in the intensity of scattered light caused by the Brownian motion of the particles are analyzed. This way, the hydrodynamic radius (Rh), which provides information about the size of the particle in its solvated state, is obtained. Rh was determined from the intensity-weighted distribution (hydrodynamic diameter was given in nm then divided by two to obtain the Rh). Larger particles scatter light with more intensity than smaller particles, so the intensity distribution emphasizes the contribution of larger particles. This distribution accurately reflects the scattering intensity of the particles and provides the most reliable measure of Rh. The volume-weighted distribution was used to estimate the percentage of protein present at a given hydrodynamic radius, as this distribution represents the relative proportion of the sample volume occupied by each particle size. As no other peaks were present on the volume-weighted distribution graph, WT Tau and the mutants are monodispersed. The distinction between the intensity-weighted distribution and the volume-weighted distribution is important for accurately interpreting DLS results and understanding the size distribution of particles in a solution [40]. The polydispersity index (PI) is a measure of the width of the size distribution. A PI of 0 indicates a perfectly monodisperse sample, while a PI of 1 indicates a highly polydisperse sample (Figure SI-8). Our sample PI are

comprised between 0.2 and 0.6 which confirms a relatively variability in the polydispersity, explaining the large value of confidence interval. However, the Rh of WT tau agree with those determined previously with the same methodology [41,42].

By examining the correlation function, the quality of the DLS data can be evaluated. The similarity between the intensity of scattered light at one moment in time and the intensity at a later moment is described by this correlation function. A quantitative indicator of this resemblance is the correlation coefficient, which is obtained from the correlation function. Perfect correlation is represented by a value of 1, and no correlation is represented by a value of 0. The hydrodynamic radius is then computed by analyzing the correlation function's decay to find the particles' diffusion coefficient. For a monomodal sample, a high-quality correlation function should have a sum of squares (SOS) value of less than 100 and a baseline that reaches 1.00. Additionally, it is critical to take into account possible error sources.

Correlograms show a typical decay pattern expected for a diffusing species (Figure SI-8). The correlation coefficient starts high, indicating strong initial correlation, and decays smoothly towards zero as time increases. This decay is consistent with Brownian motion of particles in solution. The provided data reaches a correlation of 0.9 and drops until reaching 0, reflecting its high quality. However, we cannot conclude on the sum of squares (SOS) which is supposed to be under 100, and the baseline which is expected to reach 1.00. The timescale of the decay (primarily between 1 and 100 microseconds) provides information about the diffusion coefficient of the Tau protein construct, and subsequently, its hydrodynamic radius. The fact that the measurement is at steady state is important for the validity of this analysis (figure SI-8).

Although DLS is primarily used for globular proteins, as it relies on calculating the hydrodynamic radius of a sphere and IDPs lack a well-defined structure, it can still provide information about conformational ensembles in IDPs and aggregation states. To study the sequence determinants of IDP compaction, Rh measurements associated with amino acid sequences of a large set of IDPs were compiled [43]. This study revealed that the main natural determinants of compaction in IDPs were the number of proline residues and the net charge [43]. Moreover, a strong correlation between the number of residues in a protein and its molecular mass determined by Rh measurements has been shown.

Analytical ultracentrifugation is a very powerful technique to characterize macromolecules or mixtures of macromolecules in solution by separating them using gravitational force, and then measuring their hydrodynamic properties. During the centrifugation, the concentration distributions of the macromolecule in the centrifugation cells change over time due to sedimentation transport. This change in concentration in the centrifugation cell is recorded over 2-3 hours and interpreted by the analysis software to determine the number of species present in the solution, their concentration, and their corresponding sedimentation coefficient [44]. The sedimentation coefficient S in Svedberg is proportional to the molecular mass of the macromolecule M and to its frictional coefficient f which provides shape information and is also linked to the hydrodynamic radius by equation 1 (see Materials and Methods section). The principal advantage of the method is that it could be used for spherical, elongated proteins or IDPs. In our study, we determine the sedimentation coefficient of WT Tau and its hydrodynamic parameters that agree with our previous determination [45]. As can be seen on Figure 3, the presence of one major peak corresponds to the tau monomer. Another species is detected at lower

sedimentation coefficient value, and a little aggregation at approximately 4S indicates as for DLS experiment a certain degree of polydispersity. This aggregation could be responsible for the larger confidence interval obtained in DLS than in AUC, because in DLS the aggregates participate largely in the scattered light intensity fluctuation.

The simple relationship $Rh = R0N^{v}$ has been used to provide remarkably good predictions; where Rh is the hydrodynamic radius, N is the number of residues in the protein, and R0 and v are constants [46]. In a random coil, v should be 0.588 [47], for globular proteins the relationship is: $R_h^{folded} = 4.92N^{0.285}$, for denatured proteins: $R_h^{denatured} = 2.33N^{0.549}$ and for IDPs: $R_h^{IDP} = 2.49N^{0.509}$ [43]. Tau, as an IDP of 441 amino acids, would have a hydrodynamic radius of 55 Å.

Despite the presence of some polydispersity in DLS and AUC experiments, the Rh obtained by both methods were similar and agreed with the theoretical one calculated above. Moreover, we demonstrated that the 16 mutations of serine/ threonine residues into alanine have no consequence on the Rh of tau, indicating that the mutant could be used to study the two phosphorylation states of tau. Curiously and interestingly, we also found that phosphorylation did not modify the Rh of tau even though its function was described to be modulated by specific phosphorylation patterns. Indeed, in a simpler mechanism, tau in Alzheimers disease is abnormally phosphorylated and detach from microtubules inducing their destabilization. This results in the accumulation of Tau within the neuronal cytosol and subsequent mislocalization within the soma, where it aggregates. During this process, the formation of pathological species and their propagation from neurons to neurons contribute to neurodegeneration. With our study, we can assume that the phosphorylation at the epitope AT8 does not induce global conformational changes of the protein and could be an example to study other pathological phosphorylations

in other Tau regions, such as those recognized by the PHF-1 antibody. By combining NMR experiments and molecular dynamics simulations, Gandhi et al. demonstrated the presence of a kink at residue 207 in pS202/pT205 phosphorylated Tau, similar to p-state 1 [15]. This local conformation was shown to be disrupted by an additional phosphorylation at pS208, similar to our p- state 2 phosphorylated Tau [16]. We can here specify that these local conformational changes have no effect on the global conformation of tau.

In their assessment of Rh using the CALVADOS FF, Pesce et al. reported the experimental value of 5.40 +/- 0.20 nm determined by Mukrasch et al. in their Figure 9 [10,30]. An error seems to have been made by both studies when reading the plot and the actual value is 5.20 +/- 0.20nm. This last value agrees well with the linear regression in concentration performed experimentally. Moreover, the experimental flexibility and curvature analyses of Mukrasch et al (their Figures 4 and 6) [30] agree qualitatively with our LCs and LFs for the wild-type. We based ourselves on the protocol by Pesce et al. and recovered similar results for the Nygaard Rh despite not using a reweighting technique. We also reach the same conclusion that KR Rh does underestimate the actual value as Nygaard et al. observed themselves [32]. This good agreement even with the different p-states tends to confirm the capacity of pCALVADOS to provide relevant CoE for multi-phosphorylated IDPs.

The lack of sensitivity of Rh to mutations, and most importantly p-states, could be interpreted as a sign that pCALVADOS cannot properly capture the effects of side-chain substitutions due to its coarse-grained nature. But the overall agreement of the calculated Rh with the experimental regression to 0 μM seems to be telling another story. It is possible that phosphorylation effects are more prominent for intermolecular interactions rather than intramolecular ones, which would explain the dependency on concentration observed on Figure 2. One should however keep in

mind the uniqueness problem of CoE, which states that, as bead-like proteic models are still fairly complex, there might exist several parameterizations and therefore several CoEs which can fit one target observable [48]. It is therefore possible that pCALVADOS generates ensembles which fit the experimental Rh but are still not biochemically accurate. To evaluate whether this is the case, we have to assess whether our CoE fits other experimental properties of multi phosphorylated IDPs.

Our calculations of LCs and LFs revealed that upon multi phosphorylations, the backbone of the Tau mutant locally adopts a more elongated and less flexible dynamics (Figure 6). This behavior was previously observed experimentally by Lasorsa et al. on the same system phosphorylated on pSer202 and pThr205 and could be assessed through comparison of the relaxation times of the phosphorylated and non-phosphorylated forms (Figure 3 of ref. [30]). This gives weight to the assumption that the CoEs produced by pCALVADOS are comparable to experiments.

We should however keep in mind that most experiments are conducted at low salt concentrations which are not biologically accurate, and effects such as salt shielding or even possible nP-collabs could play an important role on the dynamics of multi phosphorylated Tau in the context of the cell [12]. The agreement of pCALVADOS simulations with experiments at the residue scale has also been probed only qualitatively with LCs and LFs, further quantitative confirmations will be required to attest on the quality of the forcefield.

CONCLUSION

Dynamic Light Scattering (DLS) experiments and AUC experiment reveal no significant differences in the hydrodynamic properties of wild-type Tau and the non-

and AT8-phosphorylated mutants. These findings highlight that specific phosphorylation events at the AT8 epitope do not modulate the hydrodynamic radius and, potentially, the conformational ensemble of tau, but modulate only local conformation and give us useful information for further investigation.

Experimental results of Rh determination by DLS and UCA were completed and compatible with simulations performed with a new forcefield specifically aimed at phosphorylated IDPs by combining the CALVADOS 2 forcefield and phospho-residues parameters by Perdikari et al. [8,11].

The generated CoEs display good agreement with experimental Rh using the Nygaard method, as could be expected considering that it is targeted towards IDPs. Our calculations of Local Curvatures and Local Flexibilities confirmed that the mutations on the Tau sequence used to perform selective phosphorylations do not have a significant impact on the local dynamics. We also identified a local rigidification and extension of the epitope AT8 proportional to the number of phosphorylations qualitatively supported by several experimental results [30,48]. Long-range effects of phosphorylations were also identified, with an interesting directionality towards the N-terminal end of the tau protein.

The generation and characterization of the AT8 tau mutants have laid the groundwork for future studies aimed at elucidating the structure-function relationship of tau bound on the microtubule. This validated protein will serve as a crucial tool for subsequent studies aimed at establishing a structure-activity relationship for phosphorylations within the AT8 epitope, with a particular focus on residue S208 which was shown to trigger pathological states. By systematically investigating the effects of phosphorylation at this site on Tau's stability, and interactions with microtubules, we aim to elucidate the molecular mechanisms underlying the loss of function associated with hyperphosphorylated tau in neurodegenerative diseases.

DATA ACCESSIBILITY

Raw coarse-grained pCALVADOS trajectories and minimized all-atom trajectories are available in the following Zenodo repository along with scripts allowing the conversion: https://doi.org/10.5281/zenodo.14900596.

pCALVADOS parameters and a jupyter notebook allowing to run a pCALVADOS simulation are available in the following Github repository: https://github.com/Jules-Marien/Articles/tree/main/_2025_Lohberger_Marien_pCALVADOS

ACKNOWLEDGMENTS

This work was supported by the ANR (MAGNETAU-ANR-21- CE29-0024) and by the “Initiative d’Excellence” program from the French State (Grant “DYNAMO”, ANR-11-LABX-0011-01 and grant CACSICE, ANR-11-EQPX-0008).

REFERENCES

1. Jack, C.R., Jr.; Bennett, D.A.; Blennow, K.; Carrillo, M.C.; Dunn, B.; Haeberlein, S.B.; Holtzman, D.M.; Jagust, W.; Jessen, F.; Karlawish, J.; et al. NIA-AA Research Framework: Toward a biological definition of Alzheimer's disease. *Alzheimers Dement* **2018**, *14*, 535-562, doi:10.1016/j.jalz.2018.02.018.
2. Brion, J.P.; Couck, A.M.; Passareiro, E.; Flament-Durand, J. Neurofibrillary tangles of Alzheimer's disease: an immunohistochemical study. *Journal of submicroscopic cytology* **1985**, *17*, 89-96.
3. Sillen, A.; Barbier, P.; Landrieu, I.; Lefebvre, S.; Wieruszeski, J.M.; Leroy, A.; Peyrot, V.; Lippens, G. NMR investigation of the interaction between the neuronal protein tau and the microtubules. *Biochemistry* **2007**, *46*, 3055-3064, doi:10.1021/bi061920i.
4. Goedert, M.; Spillantini, M.G.; Jakes, R.; Rutherford, D.; Crowther, R.A. Multiple isoforms of human microtubule-associated protein tau: sequences and localization in neurofibrillary tangles of Alzheimer's disease. *Neuron* **1989**, *3*, 519-526, doi:10.1016/0896-6273(89)90210-9.
5. Merino-Serrais, P.; Soria, J.M.; Arrabal, C.A.; Ortigado-Lopez, A.; Esparza, M.A.G.; Munoz, A.; Hernandez, F.; Avila, J.; DeFelipe, J.; Leon-Espinosa, G. Protein tau phosphorylation in the proline rich region and its implication in the progression of Alzheimer's disease. *Exp. Neurol.* **2025**, *383*, 115049, doi:10.1016/j.expneurol.2024.115049.
6. Kapcha, L.H.; Rossky, P.J. A simple atomic-level hydrophobicity scale reveals protein interfacial structure. *J. Mol. Biol.* **2014**, *426*, 484-498, doi:10.1016/j.jmb.2013.09.039.
7. Tesei, G.; Schulze, T.K.; Crehuet, R.; Lindorff-Larsen, K. Accurate model of liquid– liquid phase behavior of intrinsically disordered proteins from optimization of single-chain

properties. *Proceedings of the National Academy of Sciences* **2021**, *118*, e2111696118, doi:doi:10.1073/pnas.2111696118.
8. Tesei, G.; Lindorff-Larsen, K. Improved predictions of phase behaviour of intrinsically disordered proteins by tuning the interaction range. *Open Res Eur* **2022**, *2*, 94, doi:10.12688/openreseurope.14967.2.
9. Tesei, G.; Trolle, A.I.; Jonsson, N.; Betz, J.; Knudsen, F.E.; Pesce, F.; Johansson, K.E.; Lindorff-Larsen, K. Conformational ensembles of the human intrinsically disordered proteome. *Nature* **2024**, *626*, 897-904, doi:10.1038/s41586-023-07004-5.
10. Pesce, F.; Newcombe, E.A.; Seiffert, P.; Tranchant, E.E.; Olsen, J.G.; Grace, C.R.; Kragelund, B.B.; Lindorff-Larsen, K. Assessment of models for calculating the hydrodynamic radius of intrinsically disordered proteins. *Biophys. J.* **2023**, *122*, 310-321, doi:10.1016/j.bpj.2022.12.013.
11. Perdikari, T.M.; Jovic, N.; Dignon, G.L.; Kim, Y.C.; Fawzi, N.L.; Mittal, J. A predictive coarse-grained model for position-specific effects of post-translational modifications. *Biophys. J.* **2021**, *120*, 1187-1197, doi:10.1016/j.bpj.2021.01.034.
12. Marien, J.; Prevost, C.; Sacquin-Mora, S. nP-Collabs: Investigating Counterion-Mediated Bridges in the Multiply Phosphorylated Tau-R2 Repeat. *J Chem Inf Model* **2024**, *64*, 6570-6582, doi:10.1021/acs.jcim.4c00742.
13. Malia, T.J.; Teplyakov, A.; Ernst, R.; Wu, S.J.; Lacy, E.R.; Liu, X.; Vandermeeren, M.; Mercken, M.; Luo, J.; Sweet, R.W.; et al. Epitope mapping and structural basis for the recognition of phosphorylated tau by the anti-tau antibody AT8. *Proteins* **2016**, *84*, 427-434, doi:10.1002/prot.24988.
14. Braak, H.; Alafuzoff, I.; Arzberger, T.; Kretzschmar, H.; Del Tredici, K. Staging of Alzheimer disease-associated neurofibrillary pathology using paraffin sections and immunocytochemistry. *Acta Neuropathol* **2006**, *112*, 389-404, doi:10.1007/s00401-006-0127-z.
15. Gandhi, N.S.; Landrieu, I.; Byrne, C.; Kukic, P.; Amniai, L.; Cantrelle, F.X.; Wieruszeski, J.M.; Mancera, R.L.; Jacquot, Y.; Lippens, G. A Phosphorylation-Induced Turn Defines the Alzheimer's Disease AT8 Antibody Epitope on the Tau Protein. *Angew Chem Int Ed Engl* **2015**, *54*, 6819-6823, doi:10.1002/anie.201501898.
16. Despres, C.; Byrne, C.; Qi, H.; Cantrelle, F.X.; Huvent, I.; Chambraud, B.; Baulieu, E.E.; Jacquot, Y.; Landrieu, I.; Lippens, G.; et al. Identification of the Tau phosphorylation pattern that drives its aggregation. *Proc. Natl. Acad. Sci. U. S. A.* **2017**, *114*, 9080-9085, doi:10.1073/pnas.1708448114.
17. De Bessa, T.; Breuzard, G.; Allegro, D.; Devred, F.; Peyrot, V.; Barbier, P. Tau Interaction with Tubulin and Microtubules: From Purified Proteins to Cells. In *Tau Protein: Methods and Protocols*, Smet-Nocca, C., Ed.; Springer New York: New York, NY, 2017; pp. 61-85.
18. Martinho, M.; Allegro, D.; Huvent, I.; Chabaud, C.; Etienne, E.; Kovacic, H.; Guigliarelli, B.; Peyrot, V.; Landrieu, I.; Belle, V.; et al. Two Tau binding sites on tubulin revealed by thiol-disulfide exchanges. *Scientific reports* **2018**, *8*, 13846, doi:10.1038/s41598-018-32096-9.
19. El Hajjar, L.; Bridot, C.; Nguyen, M.; Cantrelle, F.X.; Landrieu, I.; Smet-Nocca, C. Phosphorylation of Tau Protein by CDK2/cyclin A and GSK3beta Recombinant Kinases: Analysis of Phosphorylation Patterns by Nuclear Magnetic Resonance Spectroscopy. *Methods Mol Biol* **2024**, *2754*, 271-306, doi:10.1007/978-1-0716-3629-9_15.
20. Schuck, P. Size-Distribution Analysis of Macromolecules by Sedimentation Velocity Ultracentrifugation and Lamm Equation Modeling. *Biophysical Journal* **2000**, *78*, 1606-1619, doi:10.1016/S0006-3495(00)76713-0.

21. Philo, J.S. SEDNTERP: a calculation and database utility to aid interpretation of analytical ultracentrifugation and light scattering data. *Eur. Biophys. J.* **2023**, *52*, 233-266, doi:10.1007/s00249-023-01629-0.
22. Rotkiewicz, P.; Skolnick, J. Fast procedure for reconstruction of full-atom protein models from reduced representations. *J. Comput. Chem.* **2008**, *29*, 1460-1465, doi:10.1002/jcc.20906.
23. Humphrey, W.; Dalke, A.; Schulten, K. VMD: visual molecular dynamics. *J. Mol. Graph.* **1996**, *14*, 33-38, 27-38.
24. Huang, J.; Rauscher, S.; Nawrocki, G.; Ran, T.; Feig, M.; de Groot, B.L.; Grubmuller, H.; MacKerell, A.D., Jr. CHARMM36m: an improved force field for folded and intrinsically disordered proteins. *Nat Methods* **2017**, *14*, 71-73, doi:10.1038/nmeth.4067.
25. Phillips, J.C.; Hardy, D.J.; Maia, J.D.C.; Stone, J.E.; Ribeiro, J.V.; Bernardi, R.C.; Buch, R.; Fiorin, G.; Henin, J.; Jiang, W.; et al. Scalable molecular dynamics on CPU and GPU architectures with NAMD. *J. Chem. Phys.* **2020**, *153*, 044130, doi:10.1063/5.0014475.
26. Gowers, J.; Linke; Barnoud; Reddy, J.E.; Melo, N.; Seyler, L.; Domański; Dotson, L.; Buchoux; Kenney, M. MDAnalysis: A Python Package for the Rapid Analysis of Molecular Dyna mics Simulations. pp. 98 - 105.
27. Michaud-Agrawal, N.; Denning, E.J.; Woolf, T.B.; Beckstein, O. MDAnalysis: A toolkit for the analysis of molecular dynamics simulations. *J. Comput. Chem.* **2011**, *32*, 2319-2327, doi:https://doi.org/10.1002/jcc.21787.
28. McGibbon, Robert T.; Beauchamp, Kyle A.; Harrigan, Matthew P.; Klein, C.; Swails, Jason M.; Hernández, Carlos X.; Schwantes, Christian R.; Wang, L.-P.; Lane, Thomas J.; Pande, Vijay S. MDTraj: A Modern Open Library for the Analysis of Molecular Dynamics Trajectories. *Biophysical Journal* **2015**, *109*, 1528-1532, doi:10.1016/j.bpj.2015.08.015.
29. Virtanen, P.; Gommers, R.; Oliphant, T.E.; Haberland, M.; Reddy, T.; Cournapeau, D.; Burovski, E.; Peterson, P.; Weckesser, W.; Bright, J.; et al. SciPy 1.0: fundamental algorithms for scientific computing in Python. *Nat. Methods* **2020**, *17*, 261-272, doi:10.1038/s41592-019-0686-2.
30. Mukrasch, M.D.; Bibow, S.; Korukottu, J.; Jeganathan, S.; Biernat, J.; Griesinger, C.; Mandelkow, E.; Zweckstetter, M. Structural polymorphism of 441-residue tau at single residue resolution. *PLoS Biol* **2009**, *7*, e34, doi:10.1371/journal.pbio.1000034.
31. Prince, P.R.; Hochmair, J.; Brognaro, H.; Gevorgyan, S.; Franck, M.; Schubert, R.; Lorenzen, K.; Yazici, S.; Mandelkow, E.; Wegmann, S.; et al. Initiation and modulation of Tau protein phase separation by the drug suramin. *Scientific reports* **2023**, *13*, 3963, doi:10.1038/s41598-023-29846-9.
32. Nygaard, M.; Kragelund, B.B.; Papaleo, E.; Lindorff-Larsen, K. An Efficient Method for Estimating the Hydrodynamic Radius of Disordered Protein Conformations. *Biophys. J.* **2017**, *113*, 550-557, doi:10.1016/j.bpj.2017.06.042.
33. Cheek, S.; Zhang, H.; Grishin, N.V. Sequence and structure classification of kinases. *J. Mol. Biol.* **2002**, *320*, 855-881, doi:10.1016/s0022-2836(02)00538-7.
34. Noble, W.; Hanger, D.P.; Miller, C.C.; Lovestone, S. The importance of tau phosphorylation for neurodegenerative diseases. *Front Neurol* **2013**, *4*, 83, doi:10.3389/fneur.2013.00083.
35. Kimura, T.; Sharma, G.; Ishiguro, K.; Hisanaga, S.I. Phospho-Tau Bar Code: Analysis of Phosphoisotypes of Tau and Its Application to Tauopathy. *Front Neurosci* **2018**, *12*, 44, doi:10.3389/fnins.2018.00044.
36. Lefèvre, F.; Rémy, M.-H.; Masson, J.-M. Alanine-stretch scanning mutagenesis: a simple and efficient method to probe protein structure and function. *Nucleic Acids Research* **1997**, *25*, 447-448, doi:10.1093/nar/25.2.447.

37. Lee, K.-H.; Kuczera, K. Simulation analysis of selective alanine mutation effect on stability of human prion protein. *J. Biomol. Struct. Dyn.* **2023**, *41*, 2619-2629, doi:10.1080/07391102.2022.2036237.
38. Kozeleková, A.; Náplavová, A.; Brom, T.; Gašparik, N.; Šimek, J.; Houser, J.; Hritz, J. Phosphorylated and Phosphomimicking Variants May Differ—A Case Study of 14-3-3 Protein. *Frontiers in Chemistry* **2022**, *10*, doi:10.3389/fchem.2022.835733.
39. Salvi, N.; Abyzov, A.; Blackledge, M. Solvent-dependent segmental dynamics in intrinsically disordered proteins. *Sci Adv* **2019**, *5*, eaax2348, doi:10.1126/sciadv.aax2348.
40. Gast, K.; Fiedler, C. Dynamic and static light scattering of intrinsically disordered proteins. *Methods Mol Biol* **2012**, *896*, 137-161, doi:10.1007/978-1-4614-3704-8_9.
41. Flach, K.; Hilbrich, I.; Schiffmann, A.; Gartner, U.; Kruger, M.; Leonhardt, M.; Waschipky, H.; Wick, L.; Arendt, T.; Holzer, M. Tau oligomers impair artificial membrane integrity and cellular viability. *The Journal of biological chemistry* **2012**, *287*, 43223-43233, doi:10.1074/jbc.M112.396176.
42. Prince, P.R.; Hochmair, J.; Brognaro, H.; Gevorgyan, S.; Franck, M.; Schubert, R.; Lorenzen, K.; Yazici, S.; Mandelkow, E.; Wegmann, S.; et al. Initiation and modulation of Tau protein phase separation by the drug suramin. *Scientific reports* **2023**, *13*, 3963, doi:10.1038/s41598-023-29846-9.
43. Marsh, J.A.; Forman-Kay, J.D. Sequence Determinants of Compaction in Intrinsically Disordered Proteins. *Biophysical Journal* **2010**, *98*, 2383-2390, doi:10.1016/j.bpj.2010.02.006.
44. Demeler, B. Methods for the Design and Analysis of Analytical Ultracentrifugation Experiments. *Curr Protoc* **2024**, *4*, e974, doi:10.1002/cpz1.974.
45. Devred, F.; Barbier, P.; Douillard, S.; Monasterio, O.; Andreu, J.M.; Peyrot, V. Tau induces ring and microtubule formation from alphabeta-tubulin dimers under nonassembly conditions. *Biochemistry* **2004**, *43*, 10520-10531, doi:10.1021/bi0493160.
46. Kohn, J.E.; Millett, I.S.; Jacob, J.; Zagrovic, B.; Dillon, T.M.; Cingel, N.; Dothager, R.S.; Seifert, S.; Thiyagarajan, P.; Sosnick, T.R.; et al. Random-coil behavior and the dimensions of chemically unfolded proteins. *Proc. Natl. Acad. Sci. U. S. A.* **2004**, *101*, 12491-12496, doi:10.1073/pnas.0403643101.
47. Wilkins, D.K.; Grimshaw, S.B.; Receveur, V.; Dobson, C.M.; Jones, J.A.; Smith, L.J. Hydrodynamic radii of native and denatured proteins measured by pulse field gradient NMR techniques. *Biochemistry* **1999**, *38*, 16424-16431, doi:10.1021/bi991765q.
48. Lasorsa, A.; Merzougui, H.; Cantrelle, F.-X.; Sicoli, G.; Dupré, E.; Hanoulle, X.; Belle, V.; Smet-Nocca, C.; Landrieu, I. Magnetic resonance investigation of conformational responses of tau protein to specific phosphorylation. *Biophys. Chem.* **2024**, *305*, 107155, doi:https://doi.org/10.1016/j.bpc.2023.107155.